Projections of rising heat stress over the western Maritime Continent from dynamically downscaled climate simulations

Eun-Soon Im[a], Suchul Kang[b,*], Elfatih A.B. Eltahir[c]

[a] Department of Civil and Environmental Engineering/Division of Environment and Sustainability, The Hong Kong University of Science and Technology, Hong Kong
[b] Singapore-MIT Alliance for Research and Technology (SMART), Center for Environmental Sensing and Modeling (CENSAM), Singapore
[c] Ralph M. Parsons Laboratory, Massachusetts Institute of Technology, USA

ARTICLE INFO

Editor: Haywood Alan

ABSTRACT

This study assesses the future changes in heat stress in response to different emission scenarios over the western Maritime Continent. To better resolve the region-specific changes and to enhance the performance in simulating extreme events, the MIT Regional Climate Model with a 12-km horizontal resolution is used for the dynamical downscaling of three carefully selected CMIP5 global projections forced by two Representative Concentration Pathway (RCP4.5 and RCP8.5) scenarios. Daily maximum wet-bulb temperature (TW_{max}), which includes the effect of humidity, is examined to describe heat stress as regulated by future changes in temperature and humidity. An ensemble of projections reveals robust pattern in which a large increase in temperature is accompanied by a reduction in relative humidity but a significant increase in wet-bulb temperature. This increase in TW_{max} is relatively smaller over flat and coastal regions than that over mountainous region. However, the flat and coastal regions characterized by warm and humid present-day climate will be at risk even under modest increase in TW_{max}. The regional extent exposed to higher TW_{max} and the number of days on which TW_{max} exceeds its threshold value are projected to be much higher in RCP8.5 scenario than those in RCP4.5 scenario, thus highlighting the importance of controlling greenhouse gas emissions to reduce the adverse impacts on human health and heat-related mortality.

1. Introduction

The deadly heat waves that have recently occurred worldwide have raised public awareness and concern about their destructive impacts on the heat-related morbidity and mortality as well as economic losses caused by crop failures and water and energy shortages (IPCC, 2007; Wilbanks et al., 2012; LeComte, 2014; Im et al., 2017a, 2017b). Given that the detection and attribution studies on recent climate change strongly support the anthropogenic influences on severe heat waves (Knutson and Ploshay, 2016; Lewis and Karoly, 2013; Fischer and Knutti, 2015), it is reasonable to expect that continuous increases in the concentration of greenhouse gases (GHGs) will further worsen heat stress in the future.

The Coupled Model Inter-comparison Project Phase 5 (CMIP5) multimodel projections forced by elevated GHG concentration show a robust pattern of temperature increase with well-established geographical patterns that are retained over time and across emission scenarios. It is very likely that the higher latitudes of the Northern Hemisphere will continue to experience substantial warming because of

anthropogenic emission forcing (IPCC, 2012). In this regard, the tropics, particularly the Maritime Continent, where the magnitude of warming is smaller than the global mean temperature increase (Stocker et al., 2013; see Box TS.6, Fig. 1), have paid relatively less attention to climate change in terms of extreme hot temperature and related heat stress. However, less warming does not necessarily imply that the negative impacts of global warming are accordingly alleviated. Here, we describe three reasons for the tropics' high susceptibility to global warming.

First, in the tropics, the temperature increase expected from anthropogenic emission forcing is large relative to the model uncertainty and the natural variability (Hawkins and Sutton, 2009). Therefore, the signal-to-noise ratio for changes in surface temperature is the highest in the tropics, leading to the lowest uncertainty of temperature projections compared to that in other regions. This is because the background "noise" induced by internal variability is lower in the tropics than elsewhere around the world (Harrington et al., 2016). However, the high latitudes where the largest anthropogenic warming is expected are also characterized by large variability, which may delay the emergence
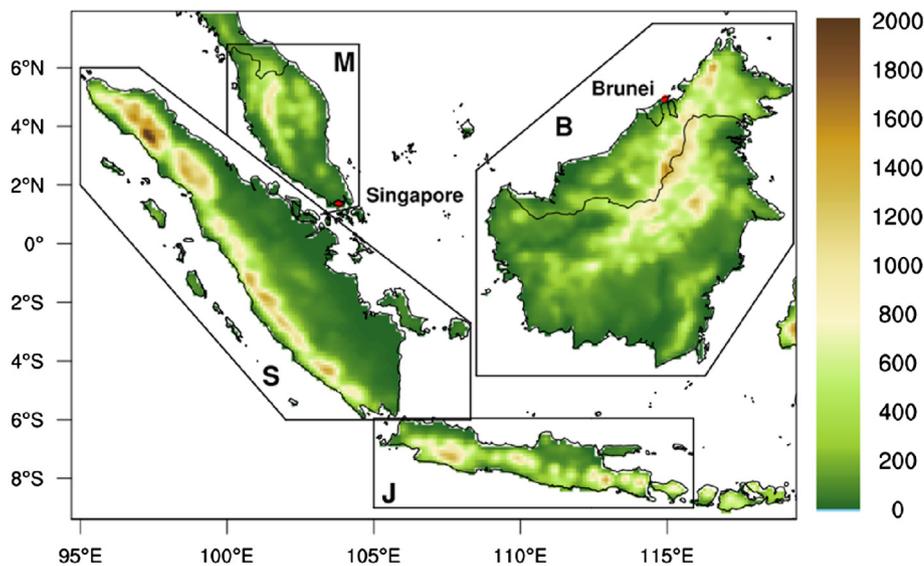
Fig. 1. Domain and topography (unit: m) used for the MRCM simulation. Land areas are divided into four subregions for detailed regional analysis (M: Malay, S: Sumatra, B: Borneo, and J: Java). Two red dots indicate the in situ observational locations within Singapore and Brunei that are used to validate the daily maximum temperature and the daily maximum wet-bulb temperature. (For interpretation of the references to color in this figure legend, the reader is referred to the web version of this article.)

of significant changes compared to internal climate variability. Furthermore, Hawkins and Sutton (2009) demonstrated that the model uncertainty measured by inter-model difference has a clear maximum at high latitudes. On contrary, the low-latitude countries around tropical areas exhibit the most imminent and robust emergence of hot temperature extremes (Diffenbaugh and Scherer, 2011; King et al., 2015; Mahlstein et al., 2011). This contrasts with the general consensus that high latitudes show the most accelerated warming in response to the increases in GHG concentration.

Second, the humid and hot tropical climate in the present day is particularly vulnerable to the increasing temperature because even modest warming may exceed the critical level of heat stress and become more dangerous and intolerable. In the absence of much seasonal temperature variation in the subequatorial zone, warm days can last almost all the year round. Although people living in these climatic conditions are relatively well acclimatizing to heat stress, there is a limit to acclimatization, which will place upper boundaries on human heat tolerance. Willett and Sherwood (2012) demonstrated that heat events may worsen more in humid tropical regions even if it warms less than the global average, due to greater absolute humidity increases. Therefore, the necessary heat acclimatization may exceed human tolerance, particularly in warm and humid tropical regions under global warming.

Finally, poor populations in areas of low socioeconomic status such as the majority of Indonesia and Malaysia rural areas will be more likely to be adversely affected by extreme heat events. The risk arising from heat stress is a function of both heat wave intensity and the vulnerability of populations influenced by socioeconomic factors (IPCC, 2012). The capacity to adopt and manage the risks of extreme heat is often limited in the tropics (IPCC, 2007). For example, limited access to air conditioning, underdeveloped infrastructure, and less-effective public health systems will greatly amplify the human vulnerability to heat stress.

Despite these foreseeable risks, few studies have comprehensively analyzed heat stress under global warming over the Maritime Continent. To the best of our knowledge, there is only minimal literature on the potential impact of climate changes on heat stress over the Maritime Continent, taking the humidity effect into consideration and using the high-resolution regional climate model (RCM) projections based on multiple global climate models (GCMs) and multiple emission forcings (e.g., RCP4.5 and RCP8.5). Recently, the unprecedented number of climate projections that have been produced within the framework of CMIP5 may provide the most reliable source of information in terms of anthropogenic climate change. However, GCM

simulations suffer a significant disadvantage in simulating key climate features over the Maritime Continent (Im and Eltahir, 2017; Kang et al., 2018). Their coarse resolution is not appropriate to resolve the distinct geographical characteristics and to capture climate extremes at small spatial scales. In this regard, we produce fine-scale climate change projections focusing on the western Maritime Continent to investigate the impact of climate change in response to the different levels of emission forcing (RCP4.5 vs. RCP8.5). The three GCM projections participating in CMIP5 that are carefully selected are dynamically downscaled using the latest version of the Massachusetts Institute of Technology (MIT) regional climate model (MRCM). The MRCM simulations with greater regional details (horizontal resolution of 12 km) can increase the value of GCM projections with relatively coarse grids. While Kang et al. (2018) assessed rainfall changes using these high-resolution climate projections, in this study, we emphasize the detailed aspects of extreme hot temperature and resultant heat stress induced by anthropogenic GHG forcings.

2. Experimental design and analysis method

2.1. MRCM experimental design

To better resolve the region-specific changes in terms of geographical patterns and severity of heat stress over the Maritime Continent, the MRCM is used for the dynamical downscaling of global climate projections forced by two Representative Concentration Pathway (RCP4.5 and RCP8.5) scenarios. The MRCM is based on the Abdus Salam International Centre for Theoretical Physics Regional Climate Model Version 3 (RegCM3, Pal et al., 2007), but with several important improvements such as land surface scheme and convection scheme (Im et al., 2014). In particular, Im and Eltahir (2017) applied the MRCM to the western Maritime Continent (same domain as this study, see Fig. 1) and demonstrated that the MRCM with a 12-km horizontal resolution shows reasonable performance in reproducing the rainfall and low-level circulation that vary diurnally and regionally. Therefore, we adopt the same version of the MRCM used by them.

The initial and boundary conditions used to force the MRCM are taken from CMIP5 participant models. Because the RCM simulation strongly depends on the GCM performance, careful selection of the best GCMs is important in the case that a limited number of GCMs are used due to computational burden. In this study, three GCMs are selected based on the stepwise screening process, including the rigorous evaluation of the performance in simulating key climate variables for the historical period over the target domain. More specifically, we first

select 19 GCMs out of 28 CMIP5 participant models based on the results of McSweeney et al. (2015) that showed reasonable performance of 19 GCMs capturing the significant climate features over the region of Southeast Asia including the Maritime Continent. We then exclude the GCMs with relatively coarser horizontal resolution of atmospheric (coarser than 2°) and oceanic (coarser than 1.2°) models, and this selection process leaves only six GCMs from the first 19 selected GCMs. Finally, the reference simulations from the selected six GCMs are evaluated focusing on the western Maritime Continent. The performances of how reasonably the models simulate rainfall, temperature, wet-bulb temperature, and humidity are assessed in terms of spatial pattern, normalized root mean square error (NRMSE), and annual cycle over land and ocean, by comparing them with Climatic Research Unit (Harris et al., 2014, hereafter referred to as CRU) and ERA Interim Reanalysis (Dee et al., 2011, hereafter referred to as ERAI) data. As a result, three GCMs are selected: Community Climate System Model Version 4 (hereafter referred to as CCSM), Australian Community Climate and Earth System Simulator Version 1.0 (hereafter referred to as ACCESS), and Max-Planck-Institution Earth System Model running on Medium Resolution grid (hereafter referred to as MPI). More detailed information for individual GCMs can be found in Table 1 of Kang et al. (2018).

Because each individual GCM provides three different simulations corresponding to the reference period (1975–2005) forced by historical GHG concentration and the future period (2070–2100) forced by RCP4.5 and RCP8.5 emission scenarios, a total of nine 31-year GCM projections are dynamically downscaled using the MRCM. After discarding the first-year MRCM simulations in both the reference and future periods as a spin-up period, 30-year projections (1975–2005 vs. 2071–2100) are analyzed.

Fig. 1 presents the domain used for the MRCM simulation. It covers the western Maritime Continent composed of four countries (Malaysia, Indonesia, Singapore, and Brunei) surrounded by vast oceans. Because the main focus of this study is to assess how the changes in temperature and humidity affect the human perception of heat stress, the analysis focuses only on land areas. For details of the regional characteristics, the land areas are divided into four subregions as indicated by the first letter of each Islands and Peninsula (M: Malay, S: Sumatra, B: Borneo, and J: Java) in Fig. 1. We simply divide these subregions based on the separate land masses rather than country basis because the land portions of Singapore and Brunei are much smaller than those of Indonesia and Malaysia. However, we validate the MRCM performance at Singapore and Brunei using in situ station observations.

2.2. Analysis method

As an effective indicator to measure extreme heat stress, we investigate changes in *TW*. Sherwood and Huber (2010) proposed the concept of a human survivability threshold based on *TW*. *TW* is defined as the temperature achieved by an air parcel if we evaporate water into it until saturation at constant pressure, therefore, it represents the combined effect of temperature and humidity. Davis et al. (2016) argued that *TW* is particularly useful in human health applications associated with heat stress because evaporation is the primary means by which bodies cool in hot environment. Increase in *TW* reduces the human body's cooling ability. Because a normal human body's temperature is maintained within a very narrow limit of ± 1 °C (Epstein and Moran, 2006), the body's inability to adjust temperature can impair physical and cognitive functions if body temperature continues to increase in levels of certain threshold (Smith et al., 2014). Unlike many other heat indices (e.g., wet-bulb globe temperature and apparent temperature) that are significantly affected by environmental, physiological, and sociological factors, *TW* establishes a clear thermodynamic limit on heat transfer that cannot be overcome by acclimatization or adaptation (Sherwood and Huber, 2010; Coffel et al., 2018). TW of 35 °C can be considered an upper limit on human survivability because

if ambient air TW exceeds 35 °C, metabolic heat can no longer be dissipated. In addition to the theoretical limit of 35 °C for human tolerance, we use the thresholds of 31 °C and 28 °C for the analysis of *TW*. Because a *TW* of 31 °C is rarely exceeded in the present climate (Sherwood and Huber, 2010), the investigation of future changes in the upper limit of historical *TW* can provide a clear insight into the consequences of global warming. Although the *TW* thresholds of 35 °C and 31 °C include the symbolic meaning, the occurrences of cases exceeding these thresholds are very limited, in particular for reference simulations. In this regard, a *TW* of 28 °C can be more realistic and practical criterion to measure thermal discomfort. Furthermore, a *TW* of 28 °C is high enough to represent extreme cases based on the observed distributions for historical period. It is demonstrated that the most common TW_{max} ranges 26–27 °C globally (Sherwood and Huber, 2010), and the land areas with the historical record of TW_{max} exceeding 28 °C are limited (Im et al., 2017b). We compute *TW* using the formulation developed by Davies-Jones (2008), which is the same method used by Pal and Eltahir (2016) and Im et al. (2017b). By using the MRCM output (temperature, relative humidity, and pressure) at 1-hour intervals, *TW* is computed on an hourly basis and then averaged over a 6-hour window because 6 h is considered the maximum duration fit humans can survive at a *TW* of 35 °C (Pal and Eltahir, 2016).

3. Results

3.1. Validation of the reference simulation

Before focusing on the future projection in response to enhanced GHG forcings, the MRCM performance in simulating the present-day climate (e.g., reference period: 1976–2005) is assessed to determine the reliability of future projections. The difficulty in validating temperature and humidity over our target region is the lack of reliable observations with high resolution at both temporal and spatial dimensions. Although ERAI is an easily available global dataset that provides many variables at subdaily time scale (e.g., 6-hour), it tends to underestimate temperature (see Fig. 2), humidity (not shown), and resultant temperature and humidity-related heat stress (see Fig. 3) over this region compared to other observations. For comparison, the CRU monthly temperature and humidity data with the resolution of 0.5° × 0.5° are used. Daily gridded observation data with a resolution of 0.25° × 0.25° generated by the APHRODITE project for Asia (Yatagai et al., 2012, hereafter referred to as APHRO) are also compared. Because there is no humidity variable in the APHRODITE project, APHRO temperature is combined with ERAI humidity and CRU humidity for comparison with the TW calculated from other datasets.

Fig. 2 presents the spatial distributions of 30-year climatology of May temperature derived from different kinds of observations and MRCM ensemble simulations. May is chosen because it is the hottest month in the annual cycle of monthly temperature over the target region. We first notice that there are significant differences among observational data. The different horizontal resolutions (ERAI: 0.75° × 0.75°, CRU: 0.5° × 0.5°, APHRO: 0.25° × 0.25°) may be responsible for their differences. Lower temperatures along the high mountainous regions and higher temperatures in the low plain and coastal regions are strongly constrained by topography. While CRU and APHRO show a similar pattern of temperature in flat areas, APHRO exhibits only the cold temperature reflecting relevant topographical modulation, leading to a sharp contrast according to the height difference. By constant, ERAI shows a much lower temperature in the regions that are warmer in CRU and APHRO observations. This is in line with the findings of Wang and Zeng (2013). Compared to station-based observations (e.g., CRU and APRHO), ERAI is found to be unsatisfactory in reproducing the surface air temperature because reanalysis temperature is strongly affected by the land surface model, the data assimilation system, and the atmospheric boundary layer turbulence parameterization (Wang and Zeng, 2013). Compared to APHRO, ERAI shows a lower
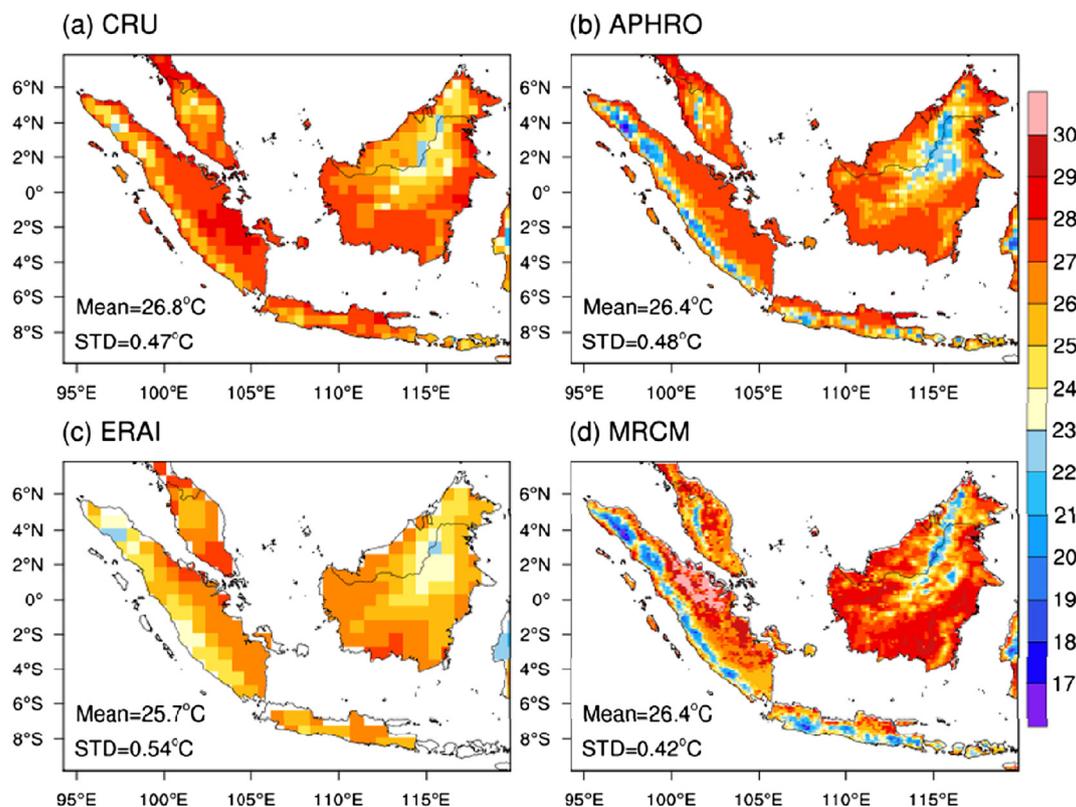
Fig. 2. Spatial distribution of 30-year climatology of mean temperature in May derived from (a) CRU, (b) APHRODITE, (c) ERA-Interim, and (d) ensemble mean of MRCM simulations. Mean and standard deviation (STD) values are calculated at each grid, and then, they are averaged over the land area.

Fig. 3. Spatial distribution of 30-year climatology of mean wet-bulb temperature in May derived from (a) CRU, (b) ERAI, (c) APHRO temperature with CRU relative humidity, (d) APHRO temperature with ERAI relative humidity, and (e) ensemble mean of MRCM simulations. Mean and standard deviation (STD) values are calculated at each grid, and then, they are averaged over the land area.
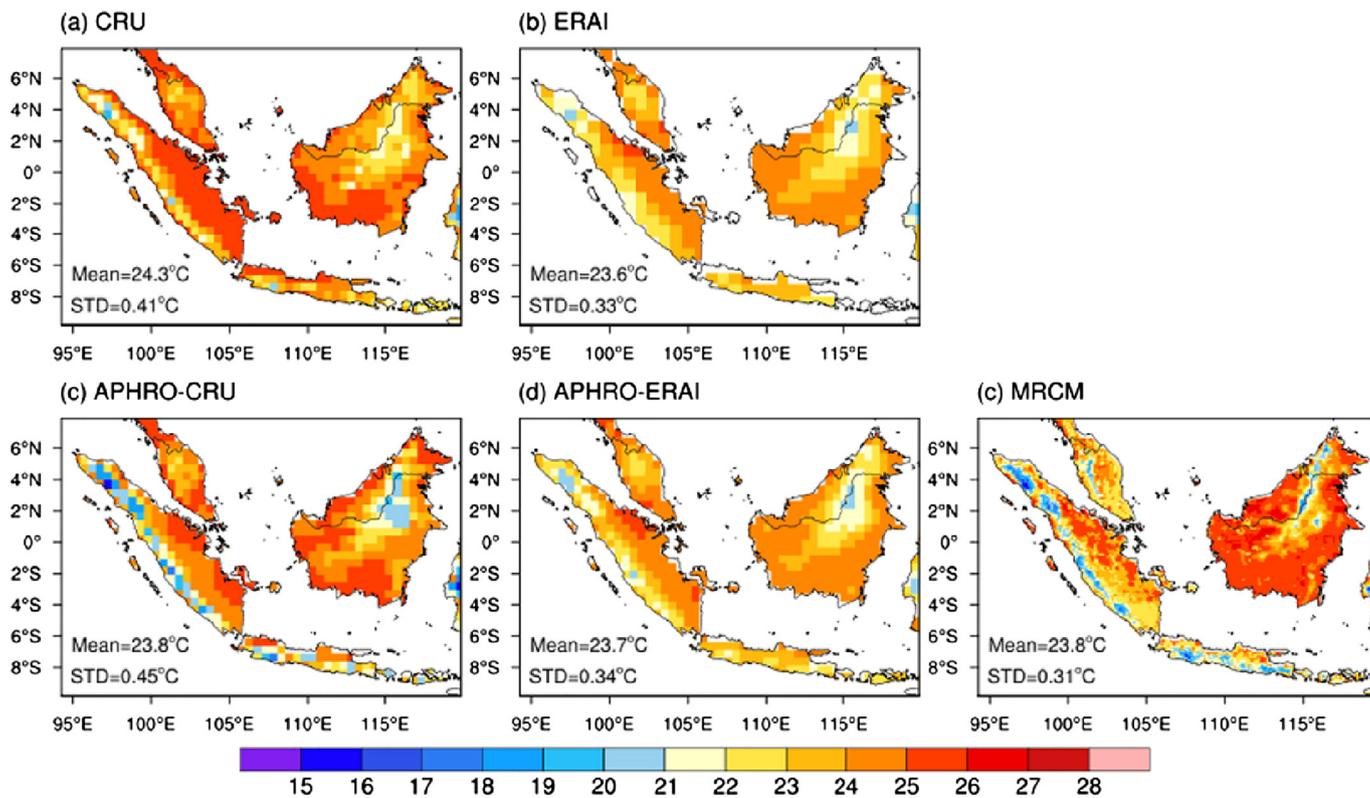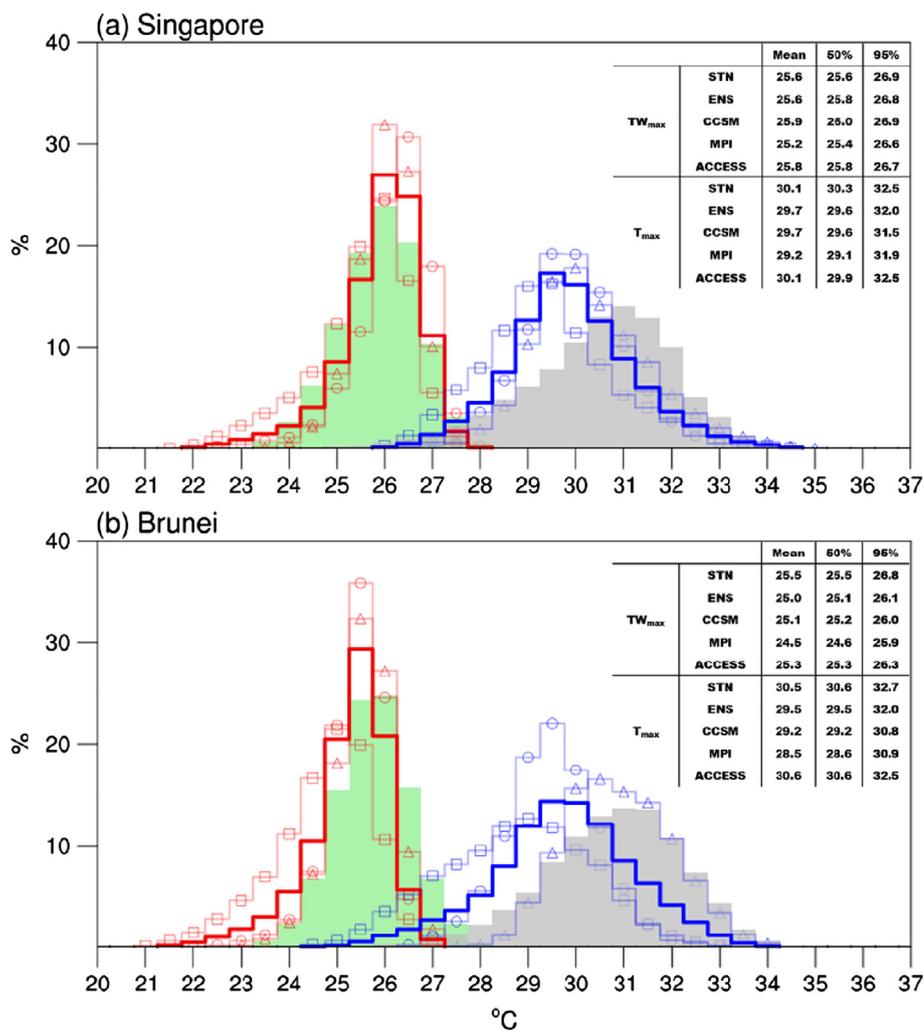
Fig. 4. Frequency distributions of daily maximum temperature (T_{max}, station observation: gray shading, MRCM simulation: thick blue line represents ENS, thin blue line with circle represents CCSM, thin blue line with square represents MPI, and thin blue line with triangle represents ACCESS) and daily maximum wet-bulb temperature (TW_{max}, station observation: yellow-green shading, MRCM simulation: thick red line represents ENS, thin red line with circle represents CCSM, thick red line with square represents MPI, and thin red line with triangle represents ACCESS) throughout the whole year during the reference period. Values within each plot indicate the mean and 50th and 95th percentile thresholds for individual distribution. (For interpretation of the references to color in this figure legend, the reader is referred to the web version of this article.)

temperature by more than 2 °C in some flat areas. Despite the visible cold bias seen in spatial pattern, the area-averaged mean temperature of ERAI does not differ greatly from those of CRU and APHRO, because the overestimated temperature in mountain regions is offset by the underestimated temperature in flat areas. In general, the ensemble mean of MRCM simulations driven by three different GCMs (CCSM, MPI, and ACCESS) is in better agreement with APHRO than with CRU or ERAI, probably because of the closer horizontal resolution. Compared to APHRO, the MRCM successfully captures the observed major characteristics in terms of regional variations and area-averaged value. As for the indicator to measure the interannual variability, the standard deviation for a 30-year reference period is also compared. The MRCM tends to slightly underestimate the interannual variability of temperature in May.

Fig. 3 presents the spatial distributions of 30-year climatology of *TW* in May. *TW*, which measures the heat stress accounting for the effect of humidity, is consistently lower than temperature by several degrees Celsius because of the evaporative cooling process. Similar to the temperature pattern, *TW* derived from ERAI is much lower than that derived from CRU over flat areas, and this problematic feature is inherited from the lower temperature seen in Fig. 2. Compared to the CRU pattern, the MRCM ensemble mean tends to overestimate *TW* in the flat regions of Borneo island, but underestimate in the southern part of Sumatra island. However, considering the uncertainty in observations with relatively low resolution, the MRCM performance is considered acceptable to project the future changes with respect to present climatic conditions. From the comparison of standard deviation, the

MRCM tends to underestimate the interannual variability of *TW* in May, similar to that observed for the temperature pattern in May. However, the MRCM can capture the lower variability range in *TW* than in temperature, which is in line with all observed or reanalysis data.

On the gross pattern of monthly mean (e.g., May) climatology of temperature and *TW*, we now focus on the detailed characteristics of daily maximum temperature (T_{max}) and daily maximum *TW* (TW_{max}) at the station level against in situ observational data. Fig. 4 presents the frequency distribution of T_{max} and TW_{max} at Changi and Brunei stations located in Singapore and Brunei, respectively. The noticeable feature at both stations is the different shapes of the T_{max} and TW_{max} distributions. Compared with T_{max} distribution, TW_{max} exhibits a narrower distribution with a lower variance and higher incidence of mean values. While T_{max} distribution has a longer upper tail exceeding 34 °C, TW_{max} shows an apparent ceiling around 28 °C, due to the inversely proportional relationship between temperature and relative humidity (Sherwood and Huber, 2010). However, note that a TW_{max} of 28 °C is already a very uncomfortable condition and TW_{max} rarely exceeds 31 °C anywhere worldwide in the present-day climate. The MRCM ensemble distribution can capture the observed pattern in terms of the different shape and position between T_{max} and TW_{max}. Importantly, the model bias is much smaller in TW_{max} than in T_{max} distribution. Despite some discrepancies regarding individual bar range (e.g., 0.5 °C interval) of TW_{max}, the MRCM shows better ability in capturing the values with highest frequency (e.g., mode) and extreme values (e.g., 95%). Because the modeled temperature and relative humidity are constrained within the thermodynamic principles, model biases in temperature can be
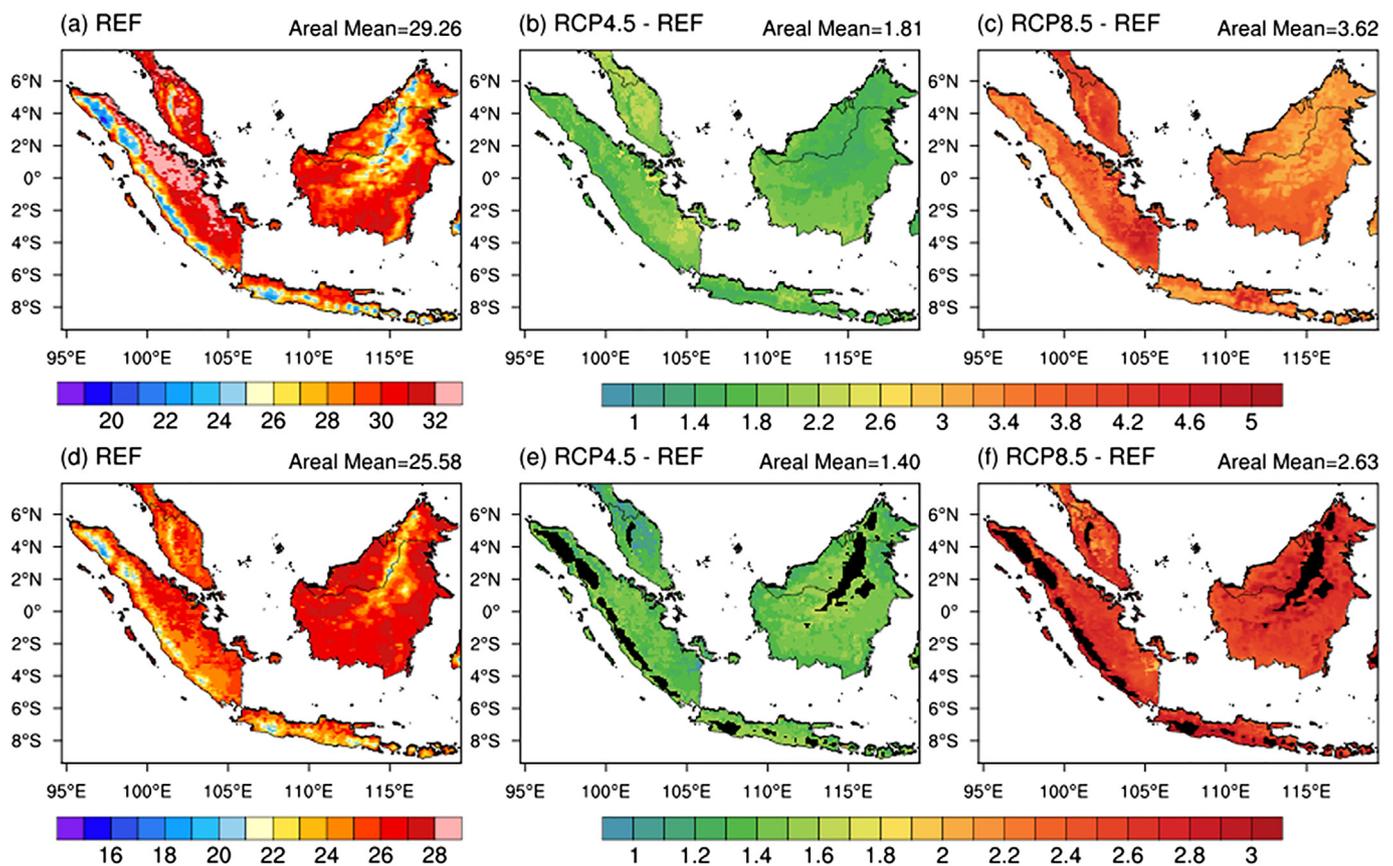
Fig. 5. Spatial distribution of 30-year climatology of T_{max} (upper panels) and TW_{max} (lower panels) for reference simulation (a, d) in May and its difference with RCP4.5 (b, e) and RCP8.5 (c, f) projections. Black shading in the distribution of TW_{max} change (e, f) indicates the areas above 650-m elevation, which are masked from the analysis.

canceled out with model biases in relative humidity when both of them are used to generate the combined quantity such as TW (Fischer and Knutti, 2012). Therefore, TW used in this study can be a more predictable indicator of heat comfort with less uncertainty, rather than solely assessing temperature or humidity. Compared to the ENS distribution, individual members show a relatively large range in their performance depending on the magnitude of systematic bias in their own climatology. However, all members show a reasonable performance in capturing the major characteristic differences between TW_{max} and T_{max}. In general, ENS is expected to outperform the individual members by smoothing out biases.

In summary, the validation of the MRCM reference simulation against various observational datasets demonstrates that the model is capable of capturing the major characteristics of long-term climatology in accordance with temperature and TW. In particular, the MRCM shows an encouraging performance in simulating the frequency distribution of daily TW_{max}, indicating a good similarity with in-situ station observations. Therefore, we estimate that MRCM projections with a high resolution (e.g., 12 km) provide a good opportunity to enhance the reliability and robustness of climate change information in terms of heat stress over the western Maritime Continent.

3.2. Projections of future changes

In this section, we focus on the future projection of heat stress based on the changes in daily TW_{max}. Fig. 5 presents the spatial distribution of climatology of T_{max} and TW_{max} in May during the reference period and their future changes under RCP4.5 and RCP8.5 scenarios at the end of the 21st century (2071–2100). The regional variations of T_{max} and TW_{max} are not greatly different from the mean temperature and mean

TW shown in Fig. 2 and 3, except that they are 2–3 °C higher. Based on our downscaled projections, the western Maritime continent will experience significant warming at a rate that is roughly proportional to the GHG forcings. T_{max} and TW_{max} are both much warmer under RCP8.5 scenario than under RCP4.5 scenario. Despite the somewhat monotonic response to emission forcing, a detailed examination of the spatial pattern reveals the crucial difference between T_{max} and TW_{max}.

For T_{max}, larger warming occurs in flat and coastal regions characterized by warm and humid present-day climate. However, the amplification of heat stress described by TW_{max} is maximum in regions where T_{max} and TW_{max} show relatively low values in the present-day climate, such as the mountainous regions. This behavior can be explained by the negatively correlated change pattern of temperature and relative humidity under global warming. According to the Clausius–Clapeyron (C–C) relationship that atmospheric moisture-holding capacity increases approximately 7% for each 1 K increase in temperature, the relative humidity of the atmosphere is expected to be largely unchanged under global warming. Although this may be true on the global scale or over open water bodies, it will not necessarily be the case over land areas because moisture sources for evapotranspiration are often limited at the regional scale (Fischer and Knutti, 2012; Giorgi et al., 2011). Indeed, our projections consistently show that the regions with a greater decrease in relative humidity coincide largely with the regions with a greater increase in T_{max}, whereas there are only small changes of increases or decreases in relative humidity over oceans (not shown).

A large reduction in relative humidity over flat and coastal regions partly acts to suppress the greater amplification of heat stress over these regions. Note that the lower amplification of TW_{max} over the flat and coastal regions should be interpreted from the relative comparison of
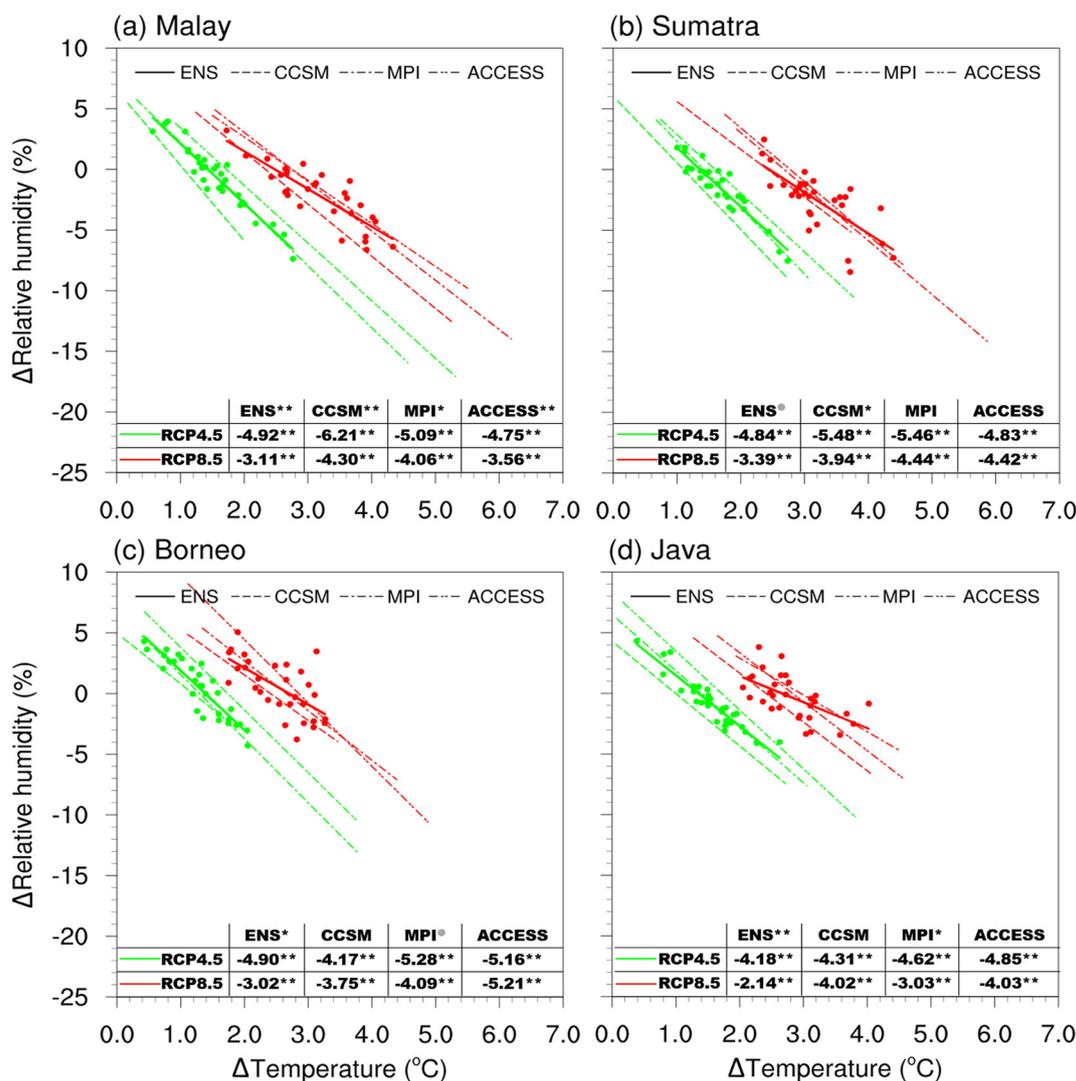
Fig. 6. Scatter plot of changes in temperature (x-axis) against changes in relative humidity (y-axis) corresponding to the occurrence of yearly maximum TW_{max} derived from RCP4.5 (marked in yellowish green) and RCP8.5 (marked in red) projections with respect to the climatological mean of corresponding variables during the reference period. While 30 points of scatterplots and thick regression line are derived from ENS averaged over the four subregions for 30 years, three individual models provide only linear regression lines without scatterplots. The values for ENS and individual models denote the coefficients of corresponding regression lines, and superscripted asterisk of values denote the significance of regression coefficient. ENS and individual models also provide the result of hypothesis test of whether the difference between the regression slopes derived from RCP4.5 and RCP8.5 is statistically significant. The gray circle, one asterisk, and two asterisks denote the statistical significance at the 90%, 95%, and 99% confidence level, respectively. (For interpretation of the references to color in this figure legend, the reader is referred to the web version of this article.)

mountainous regions where the maximum increases in TW_{max} occur. For the flat and coastal regions included in our simulation domain, TW_{max} derived from the reference simulation is much lower than the TW_{max} of 31 °C that is approximately the maximum value in the present-day climate. Therefore, the more than 2.5 °C increase in TW_{max} projected in RCP8.5 scenario is a serious hazard as it significantly narrows the gap toward the upper limit on human survivability (e.g., TW_{max} of 35 °C). On contrary, heat stress is not really relevant to the mountainous regions. More specifically, the regions above 650-m elevation mostly show TW_{max} below 24 °C for reference simulation. However, for the future climate under global warming, TW_{max} is projected to increase more in these regions than in flat regions due to the relatively less decrease (or even slight increase) in relative humidity over mountainous regions (not shown). We exclude the regions above 650 m (black shading in Fig. 5 (e, f)) in the following analysis because a large increase in TW_{max} in regions that have temperatures significantly below the critical threshold (e.g., 35 °C) is less important in terms of the risk of heat stress. We arbitrarily select 650-m elevation with the

purpose of eliminating the regions with a lower TW_{max}; however, the geographical boundaries of 600-, 650-, and 700-m elevation are so close that the sensitivity of TW_{max} to elevation selection (at least among 600, 650, and 700 m) is negligible (not shown).

To quantitatively examine the joint behavior of temperature and humidity forced by emission scenarios, we examine the relationship between changes in temperature and changes in relative humidity corresponding to the occurrence of yearly maximum TW_{max} (Fig. 6). Changes in temperature and relative humidity are calculated from RCP4.5 and RCP8.5 scenarios with respect to climatological mean during the reference period using the regionally averaged values over four subregions, namely, Malay, Sumatra, Borneo, and Java. Regardless of the region, the negative correlation of changes in temperature and relative humidity appears to be relevant, showing the statistical significance of all regression lines at the 99% confidence level. This result is generally in line with the results presented by Fischer and Knutti (2012). While temperature shows entirely positive changes, future relative humidity when the yearly maximum of TW_{max} occurs is mostly
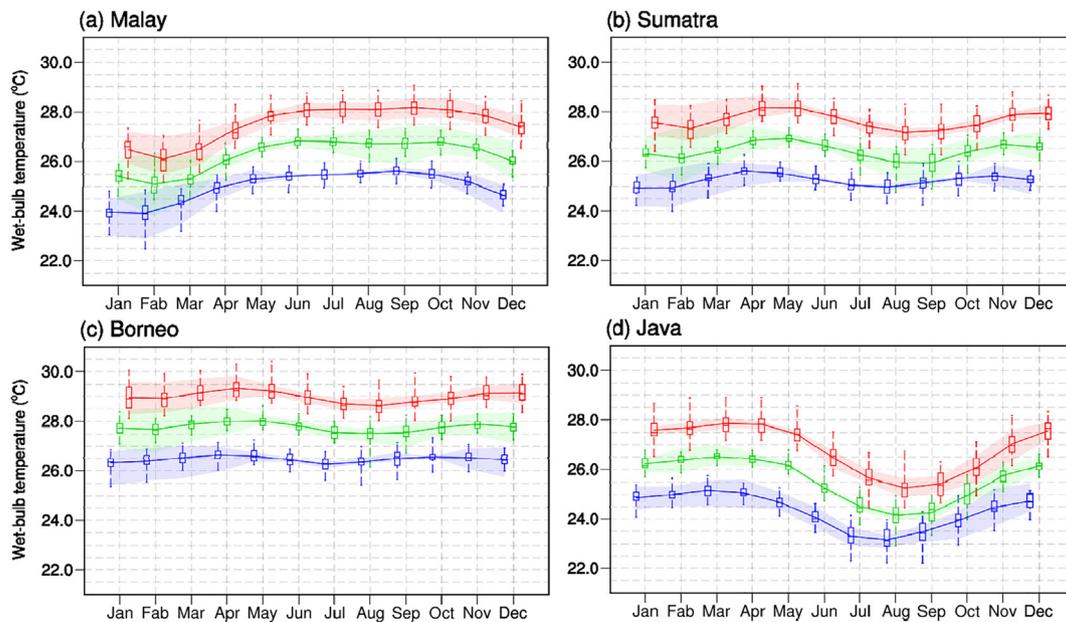
Fig. 7. Box plot of the annual cycle of the monthly mean of TW_{max} averaged over the four subregions. The blue, green, and red colors represent the reference simulation (1976–2005) and RCP4.5 and RCP8.5 projections (2071–2100), respectively. Each box plot is generated using 30 values of ENS, and the bottom and top of the box are the first (25th percentile) and third (75th percentile) quartiles, and the band inside the box is the second quartile (the median). The line connecting the 12-month data represents the 30-year mean of TW_{max} from ENS, and the shading covers the ranges for the 30-year mean of TW_{max} from three individual members. (For interpretation of the references to color in this figure legend, the reader is referred to the web version of this article.)

reduced compared to the reference period. However, the strength of the negative correlation is more weakened in RCP8.5 than in RCP4.5. We perform a hypothesis test to check whether the difference between the regression slopes derived from RCP4.5 and RCP8.5 is statistically significant. Although individual members do not show the robust behavior from a statistical viewpoint, the difference in regression slopes derived from RCP4.5 and RCP8.5 ENS is statistically significant at least at the 90% confidence level for all regions. This result supports the conclusion that the reduction in humidity seems to be plateauing, rather than continuing to decrease. For example, each subregion shows a similar range of reduction in relative humidity between RCP8.5 and RCP4.5, but a much greater increase in temperature in RCP8.5 than RCP4.5. Therefore, RCP8.5 projection can form a much more hazardous environment in terms of heat stress by a larger increase in temperature and less decrease in relative humidity.

Next, we investigate the impact of anthropogenic emission forcings on the annual cycle of the monthly mean of c averaged over four subregions (Fig. 7). The three MRCM ensemble members driven by the CCSM, MPI, and ACCESS global projections are averaged; thus, each box at a given month is generated using 30 values varying yearly for the 30-year reference and future periods. In fact, the pattern of the annual cycle does not change significantly across any region in response to enhanced GHG concentrations, but the warming from RCP4.5 and RCP8.5 emission scenarios mostly manifests itself as a shift in an annual cycle toward higher values compared to the reference climate. As demonstrated by many previous studies that assessed temperature change, TW_{max} also responds monotonically to emission forcing, showing a large sensitivity to different emission scenarios. Seemingly, greater emission forcing leads to a greater increase in TW_{max}, which is in line with the change in spatial pattern shown in Fig. 5. While the median value of TW_{max} is systematically shifted toward a higher value in a warming climate, the degree of dispersion bounded by upper and lower outliers shows rather different behaviors across emission scenarios. Compared to reference and RCP4.5 scenarios, a much larger variability appears in RCP8.5 projections. The upper ends of the whiskers are significantly increased, which is directly related to the severity of extreme events. For example, TW_{max} exceeds 30 °C over Borneo in both

April and May. As this is an area-averaged value over Borneo island (except for the regions above 650-m elevation), it is not surprising that there will be some particular locations with TW_{max} higher than 30 °C (see Fig. 8). In addition to box plot based on ENS, Fig. 7 also provides a 30-year mean of TW_{max} from ENS, and the shading covers the ranges for the 30-year mean of TW_{max} from three individual members. In general, the mean value for each month is very close to the median of box plot, but the difference is also visible for some months or regions (e.g., January and April in Malay). The inter-model spread of mean TW_{max} seems to vary according to specific month, scenario, and region, showing a lack of consistency. This implies that the sensitivity of individual ensemble members with different driving GCMs is not negligible.

Fig. 8 presents the land area fractions that are exposed to TW_{max} values at least once throughout the reference simulation and RCP4.5 and RCP8.5 projections. For example, the ENS reference simulation demonstrates that only 22% land area of Malay has experienced daily TW_{max} exceeding 27 °C. This implies that 78% land area of Malay has never experienced daily TW_{max} exceeding 27 °C for the entire 10,950 days (365-day * 30-year) of reference simulation. These calculations are performed at all grid points included in the four subregions after excluding regions above 650-m elevation. As global warming increases, the fraction of land area exposed to higher TW_{max} is projected to significantly increase. Under RCP8.5 scenario, the locations with TW_{max} above 31 °C, which is nearly equivalent to the historical maximum value of TW_{max} globally, emerge in all four subregions. In particular, ENS shows that approximately 26% of the land area in Borneo island will be exposed to TW_{max} above 31 °C. However, if the emissions are reduced to the level of RCP4.5 scenario, the exposure fraction decreases to around 2%. This huge difference (26% vs. 2%) between the projections under RCP8.5 and RCP4.5 scenarios suggests that the region stands to benefit from significant mitigation efforts. Distributions from individual members are dispersed around ENS. Therefore, certain model projections are more extreme than ENS. However, based on our projections, TW_{max} does not breach the 35 °C upper limit of human survivability in any of the locations and any of individual members considered. Nevertheless, TW_{max} above 31 °C is sufficiently high to be
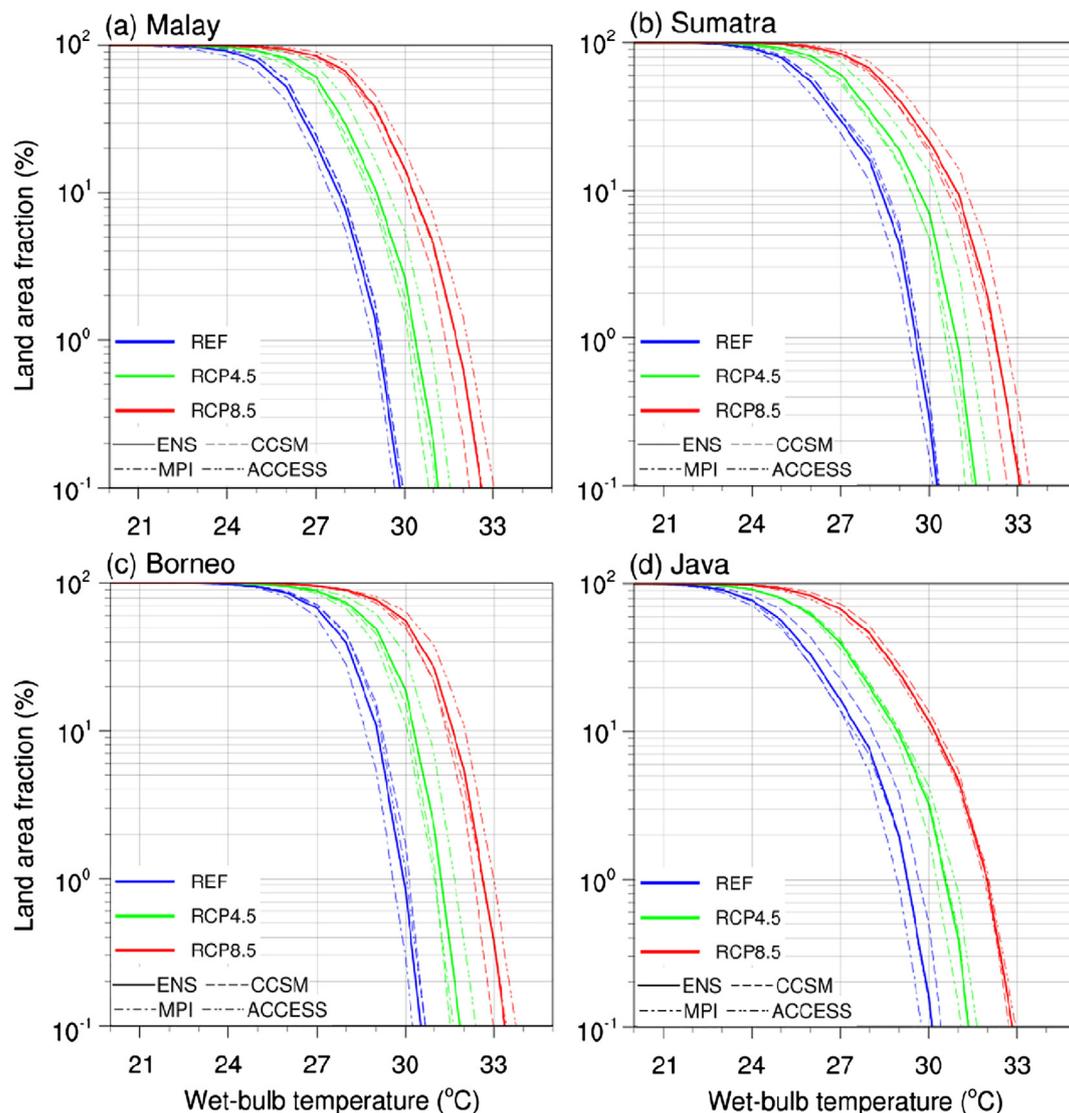
Fig. 8. Land area fractions (%) exposed to TW_{max} values at least once are displayed for the four subregions, excluding land areas above 650-m elevation. After the number of grid points that exceeded a certain threshold (e.g., 33 °C, 32 °C, 31 °C, … this value gradually decreases until the total fraction reaches 100%) are counted, their percentage with respect to the total grid points including each region (e.g., Malay) is calculated. Blue, green, and red lines represent the reference simulation (1976–2005) and RCP4.5 and RCP8.5 projections (2071–2100), respectively. The solid line represents data derived from ENS, and different types of broken lines are derived from three individual members. (For interpretation of the references to color in this figure legend, the reader is referred to the web version of this article.)

hazardous.

In addition to the exposure fraction of the regional extent, we also investigate how often physically uncomfortable days due to heat stress may arise under the different emission scenarios. Fig. 9 presents the box plot of the number of days per year with TW_{max} exceeding 28 °C threshold at all grid points included in the four subregions after excluding regions above 650–m elevation. As addressed in Section 2.2, TW_{max} of 28 °C can be a more realistic and practical criterion to measure thermal discomfort than other theoretical limits (e.g., 31 °C and 35 °C with rare incidence rates). If the majority of locations considered do not have TW_{max} exceeding the 28 °C threshold, the box that is marked by 25% (bottom) and 75% (top) value of the total data cannot be described like Malay and Java during the reference period. Again, Borneo island is particularly prone to heat stress under RCP8.5 scenario. Approximately 75% of the land area will experience more than 340 days per year with TW_{max} exceeding 28 °C. This is much higher than the equivalent value of about 20 days in the reference climate. Other regions also show similar change patterns across different scenarios, although the severity under RCP8.5 scenario is less than that of Borneo. This result implies that uncommonly high TW in the reference

simulation will become characterized as normal in the future due to global warming.

As an illustrative summary to effectively display the notable increase in heat stress under global warming, we adopt the table format of the National Weather Service Heat Index provided by the National Oceanic and Atmospheric Administration (http://www.nws.noaa.gov/om/heat/heat_index.shtml), which is very popular and provides the heat stress risk levels. The background numbers filled in the table are TW values calculated based on the temperature (x-axis, °C converted from °F) and relative humidity (y-axis, %) that are gradually increased. Within this frame, we mark temperature and relative humidity when yearly maximum TW_{max} (°C) occurs (Fig. 10). Corresponding values are averaged over the four subregions from the reference simulation and RCP4.5 and RCP8.5 projections. Because these values are obtained after area averaging, they tend to smooth out extreme values that appear in individual locations. Tracking the movement of TW_{max} corresponding to the reference simulation and RCP4.5 and RCP8.5 projections clearly shows that global warming pushes TW_{max} into an area of severe risk level. Following the risk levels categorized by the NOAA heat index, TW_{max} values during the reference period are largely positioned within
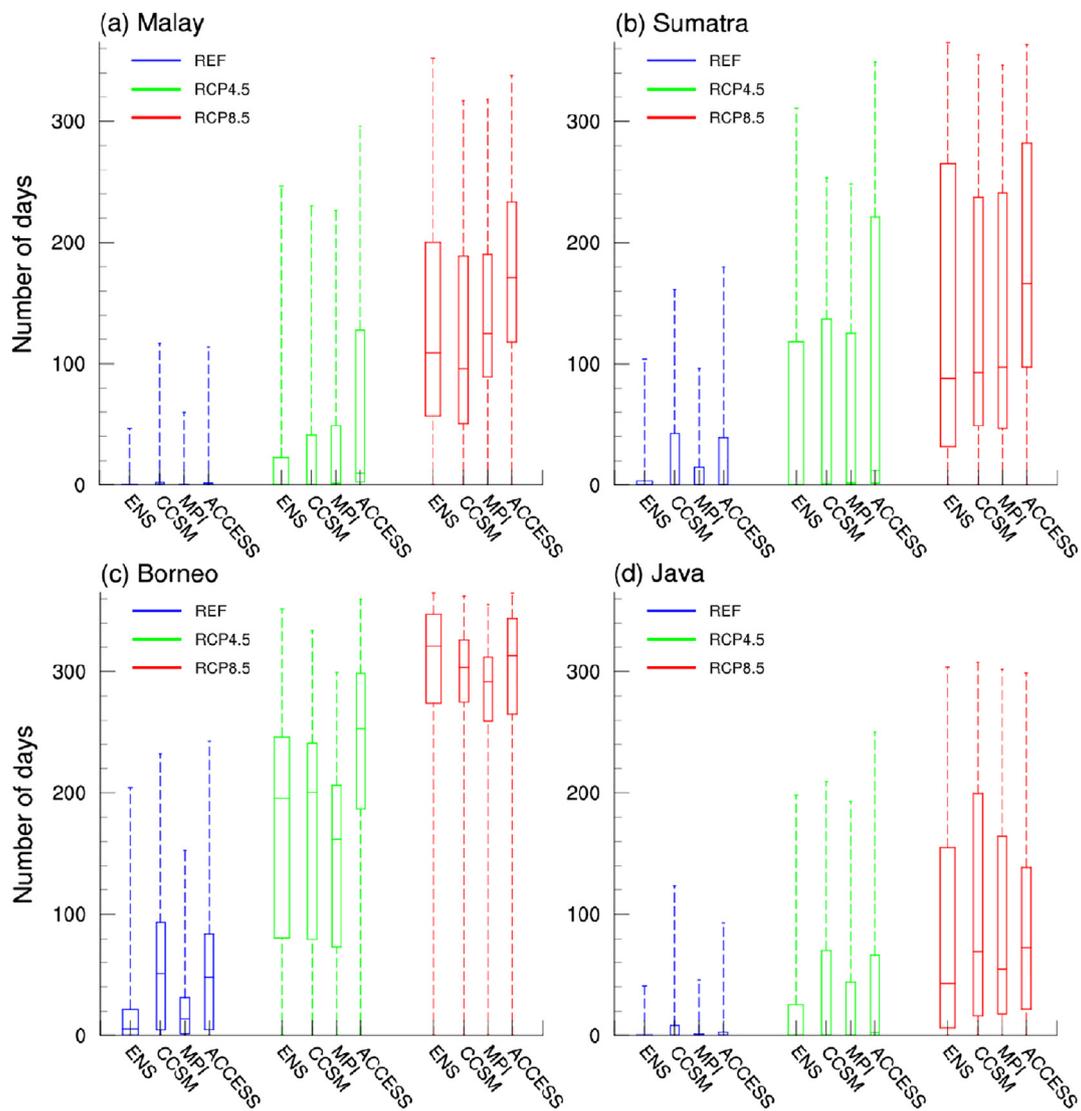
Fig. 9. Box plot of the number of days on which TW_{max} exceeds the 28 °C threshold at all grid points included in the four subregions excluding regions above 650-m elevation. For individual grid point, all days exceeding the threshold (e.g., 28 °C) are counted for 30 years, and then, the annual-based number of days is obtained by dividing the number of years (e.g., 30). Once the annual number of days exceeding threshold at all grid points are counted, they are pooled for calculating the statistics needed for box plot. Blue, green, and red lines represent the reference simulation (1976–2005) and RCP4.5 and RCP8.5 projections (2071–2100), respectively. Box plot for ENS has relatively wide width compared to those from individual models. The bottom and top of the box are the first (25th percentile) and third (75th percentile) quartiles, respectively, and the band inside the box is the second quartile (the median). The upper and lower ends of the whiskers represent the maximum and minimum of all inputted data, respectively. (For interpretation of the references to color in this figure legend, the reader is referred to the web version of this article.)

the boundary of "extreme caution" risk level. However, TW_{max} values averaged over Borneo island under RCP8.5 scenario (marked by "B" in red) appear in the "danger" risk category near the border of "extreme danger", and some values belong to the risk level categorized as "extreme danger."

Fig. 11 presents the yearly maximum of daily minimum wet-bulb temperature (TW_{min}, °C) and concurrent temperature and relative humidity in the same format as in Fig. 10. It is well known that if heat stress is accumulated without a break period, it would pose much more severe threat to human health. In this regard, the emergence of higher TW_{min} corresponding to the dangerous risk level can be an indicator for measuring the severity of heat stress and its adverse impact on human health. Compared to the characteristics of TW_{max}, TW_{min} is likely to occur under the condition of relatively lower temperature but with higher relative humidity. Based on the reference simulation, the yearly maximum TW_{min} over Malay, Sumatra, and Java poses no risk. However, the yearly maximum TW_{min} under RCP8.5 scenario increases to

the "extreme caution" risk level. Changes in the yearly maximum TW_{min} over Borneo suggest a more vulnerable situation. The risk of yearly maximum TW_{min} is expected to reach the "danger" level under RCP8.5 scenario.

4. Summary and conclusions

The study provides detailed projections of heat stress in response to the different scenarios of future GHG emissions focusing on the western Maritime Continent. To better resolve the unique geographical setting and to enhance the performance in capturing extremes, the three CMIP5 global projections that showed the best performance with respect to the reference simulation over the target region are dynamically downscaled using the MRCM with 12-km horizontal resolution. Because extreme indices measured solely by temperature are less capable of representing the typical meteorological conditions for high temperature and humidity in the tropics, wet-bulb temperature (*TW*), which
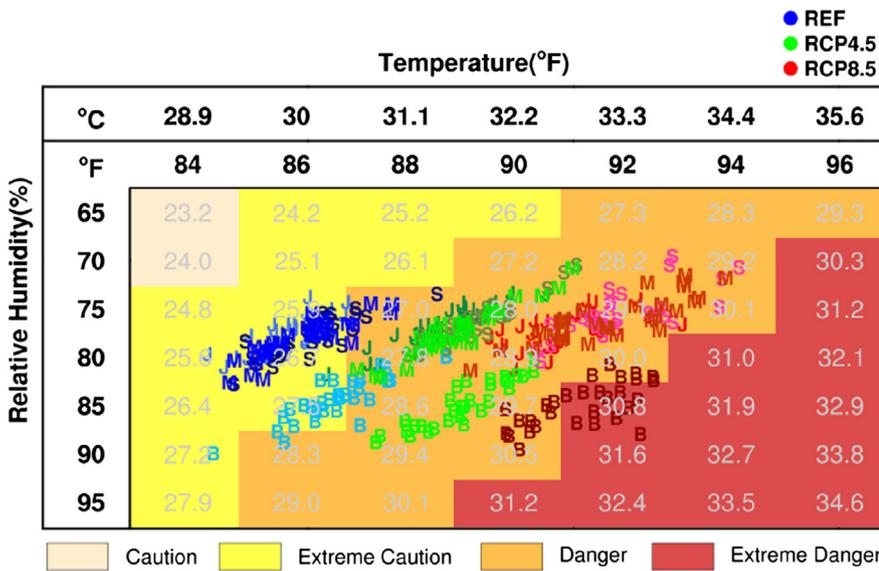
Fig. 10. Yearly maximum TW_{max} (°C) derived from the reference simulation (1976–2005) and RCP4.5 and RCP8.5 projections (2071–2100) and concurrent temperature and relative humidity corresponding to the occurrence of TW_{max}. The four heat stress risk levels adopted by NWS are indicated by different colors. M, S, B, and J indicate the values calculated from the four subregions, namely, Malay, Sumatra, Borneo, and Java, respectively. The blue, green, and red ranges are derived from the simulations forced by historical, RCP4.5, and RCP8.5 emission forcings, respectively. (For interpretation of the references to color in this figure legend, the reader is referred to the web version of this article.)
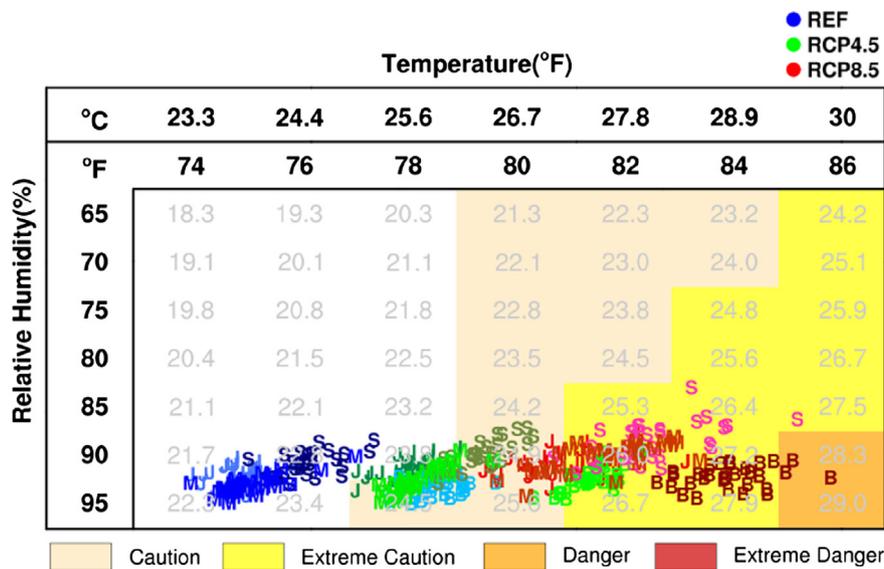

Fig. 11. As in Fig. 10 but for the yearly maximum of daily minimum wet-bulb temperature (TW_{min}, °C).

considers both, is computed on an hourly basis, and daily maximum and minimum TW picked up in the moving average value with 6-hour window is mainly analyzed.

The climatological patterns of temperature and TW derived from the MRCM high-resolution simulations during the reference period are in good agreement with observed ones, capturing locally relevant aspects along the mountainous regions or flat coast regions. An ensemble of future projections under different emission scenarios demonstrates that the level of GHG emission forcing will greatly affect the fraction of the regional extent exposed to higher TW and the number of days with higher TW. In particular, Borneo island exhibits a high sensitivity to different emission scenarios. While the extent of exposure to TW_{max} above 31 °C reaches 20% of the land area under RCP8.5 scenario, it falls to around 0.1% if the emission is reduced to RCP4.5 level. In addition, Borneo island is projected to experience a sharply increased number of days per year surpassing the TW_{max} of 28 °C under RCP8.5 scenario, indicating significant negative impacts from the business-as-usual scenario.

In this study, we do not apply any statistical method to adjust the systematic bias seen in model simulations. The most direct reason that we could not apply bias correction is because we could not find any

appropriate observational (or reanalysis) data for the calculation of correction factors. More specifically, at least 6-hour gridded temperature and humidity data over the target region are necessary for correcting simulated temperature and humidity that are used for computing the wet-bulb temperature. One potential dataset may be the ERAInterim reanalysis, but its climatological mean pattern of temperature shows a large discrepancy with other data based on ground-based observations (e.g., CRU and APHRO, see Fig. 2), which in turn leads to a severe underestimation of wet-bulb temperature along the flat regions (see Fig. 3). Therefore, bias correction based on reanalysis data characterized by a substantial level of uncertainty may introduce new errors to model simulation, resulting in misleading interpretations. Because this study mainly focuses on the robust response to the enhanced GHG emissions (i.e., RCP4.5 and RCP8.5 scenarios) in terms of heat stress, important findings are derived from the comparison of reference simulation with RCP4.5 and RCP8.5 projections under the assumption of "stationarity" that bias pattern does not change with time. For example, the mitigation impact of GHG emissions on heat stress will not be affected by bias correction in terms of qualitative aspects. However, the extreme analysis counting exceedance based on absolute threshold (e.g., 28 °C) may be affected by model bias.

A significant body of research that has analyzed historical heat waves and modeled future projections has consistently suggested that the frequency and intensity of heat waves will inevitably increase under ongoing climate change. However, most scientific publications on deadly heat waves have focused on developed mid-latitude countries (Mora et al., 2017). The risk of extreme heat stress tends to be underestimated in tropical regions, such that limited information is available for understanding the current status and preparation for future changes. While the occurrences of extreme hot temperature in mid-latitudes are concentrated only in summer due to greater seasonality, the year-round warm and humid weather of the tropics potentially aggravate the adverse impacts on human health because of the accumulation of heat stress. Furthermore, the current level of TW measured by the combination of temperature and humidity is approaching a dangerous level of heat stress (i.e., TW_{max} of 31 °C). Therefore, even without the increased temperature variability that is often emphasized as the cause of the European heat waves (e.g., Schär et al., 2004), the increases in mean temperature seen in Fig. 7 may boost the heat stress toward intolerable levels because of the combined high humidity. In fact, because the shape of daily TW_{max} distribution does not change dramatically between reference simulation and future projection (not shown), it is reasonable to consider that the increase in extreme TW_{max} is mostly due to the shift of the mean, rather than changes in variability. Well-prepared adaption strategies and action plans may assist people in alleviating the devastating consequences arising from deadly heat waves, but the absolute limit of human thermoregulatory capacity (e.g., TW of 35 °C) cannot be overcome by the adaption efforts (Mora et al., 2017; Sherwood and Huber, 2010). Therefore, an aggressive mitigation of GHGs to minimize the increases in mean temperature is more important than ever.

Acknowledgments

References

Coffel, E.D., Horton, R.M., de Sherbinin, A., 2018. Temperature and humidity based projections of a rapid rise in global heat stress exposure during the 21st century. Environ. Res. Lett. 13, 014001.

Davies-Jones, R., 2008. An efficient and accurate method for computing the wet-bulb temperature along pseudoadiabats. Mon. Weather Rev. 136, 2764–2785. http://dx.doi.org/10.1175/2007MWR2224.1.

Davis, R.E., McGregor, G.R., Enfield, K.B., 2016. Humidity: a review and primer on atmospheric moisture and human health. Environ. Res. 144, 106–116. http://dx.doi.org/10.1016/j.envres.2015.10.014.

Dee, D.P., Uppala, S.M., Simmons, A.J., Berrisford, P., Poli, P., Kobayashi, S., Andrae, U., Balmaseda, M.A., Balsamo, G., Bauer, P., Bechtold, P., Beljaars, A.C.M., van de Berg, L., Bidlot, J., Bormann, N., Delsol, C., Dragani, R., Fuentes, M., Geer, A.J., Haimberger, L., Healy, S.B., Hersbach, H., Hólm, E.V., Isaksen, L., Kållberg, P., Köhler, M., Matricardi, M., McNally, A.P., Monge-Sanz, B.M., Morcrette, J.J., Park, B.K., Peubey, C., de Rosnay, P., Tavolato, C., Thépaut, J.N., Vitart, F., 2011. The ERA-interim reanalysis: configuration and performance of the data assimilation system. Q. J. R. Meteorol. Soc. 137 (656), 553–597. http://dx.doi.org/10.1002/qj.828.

Diffenbaugh, N., Scherer, M., 2011. Observational and model evidence of global emergence of permanent, unprecedented heat in the 20th and 21st centuries. Clim. Chang. 107, 615–624.

Epstein, Y., Moran, D., 2006. Thermal comfort and the heat stress indices. Ind. Health 44, 388–398.

Fischer, E.M., Knutti, R., 2012. Robust projections of combined humidity and temperature extremes. Nat. Clim. Chang. 3, 126–130. http://dx.doi.org/10.1038/nclimate1682.

Fischer, E.M., Knutti, R., 2015. Anthropogenic contribution to global occurrence of heavy-precipitation and high-temperature extremes. Nat. Clim. Chang. 5, 560–564. http://dx.doi.org/10.1038/nclimate2617.

Giorgi, F., Im, E.-S., Coppola, E., Diffenbaugh, N.S., Gao, X.J., Mariotti, L., Shi, Y., 2011.

Higher hydroclimatic intensity with global warming. J. Clim. 24, 5309–5324.

Harrington, L.J., Frame, D.J., Fischer, E.M., Hawkins, E., Joshi, M., Jones, C.D., 2016. Poorest countries experience earlier anthropogenic emergence of daily temperature extremes. Environ. Res. Lett. 11 (5), 055007. http://dx.doi.org/10.1088/1748-9326/11/5/055007.

Harris, I., Jones, P., Osborn, T., Lister, D., 2014. Updated high-resolution grids of monthly climatic observations-the CRU TS3.10 dataset. Int. J. Climatol. 34, 623–642. http://dx.doi.org/10.1002/joc.3711.

Hawkins, E., Sutton, R., 2009. The potential to narrow uncertainty in regional climate predictions. Bull. Am. Meteorol. Soc. 90, 1095–1107. http://dx.doi.org/10.1175/2009BAMS2607.1.

Im, E.-S., Eltahir, E.A.B., 2017. Simulation of the diurnal variation of rainfall over the western Maritime Continent using the MIT regional climate model. Clim. Dyn. http://dx.doi.org/10.1007/s00382-017-3907-3.

Im, E.-S., Gianotti, R.L., Eltahir, E.A.B., 2014. Improving the simulation of the West African Monsoon using the MIT regional climate model. J. Clim. 27, 2209–2229. http://dx.doi.org/10.1175/JCLI-D-13-00188.1.

Im, E.-S., Choi, Y.-W., Ahn, J.-B., 2017a. Worsening of heat stress due to global warming in South Korea based on multi-RCM ensemble projections. J. Geophys. Res. Atmos. 122, 11444–11461. http://dx.doi.org/10.1002/2007JD026731.

Im, E.-S., Pal, J.S., Eltahir, E.A.B., 2017b. Deadly heat waves projected in the densely-populated agricultural regions of South Asia. Sci. Adv. 3, e1603322. http://dx.doi.org/10.1126/sciadv.1603322.

IPCC, 2007. Climate change 2007: the physical science basis. In: Solomon, S., Qin, D., Manning, M., Chen, Z., Marquis, M., Averyt, K.B., Tignor, M., Miller, H.L. (Eds.), Contribution of Working Group I to the Fourth Assessment Report of the Intergovernmental Panel on Climate Change. Cambridge University Press, Cambridge.

IPCC, 2012. Managing the risks of extreme events and disasters to advance climate change adaptation. In: Field, C.B., Barros, V., Stocker, T.F., Qin, D., Dokken, D.J., Ebi, K.L., Mastrandrea, M.D., Mach, D.J., Plattner, G.K., Allen, S.K., Tignor, M., Midgley, P.M. (Eds.), A Special Report of Working Groups I and II of the Intergovernmental Panel on Climate Change. Cambridge University Press, Cambridge, UK, and New York, NY, USA (582 pp).

Kang, S., Im, E.-S., Eltahir, E.A.B., 2018. Future climate change enhances rainfall seasonality in a regional model of Western Maritime Continent. Clim. Dyn. http://dx.doi.org/10.1007/s00382-017-3907-3.

King, A.D., Donat, M.G., Fischer, E.M., et al., 2015. The timing of anthropogenic emergence in simulated climate extremes. Environ. Res. Lett. 10 (94015). http://dx.doi.org/10.1088/1748-9326/10/9/094015.

Knutson, T.R., Ploshay, J.J., 2016. Detection of anthropogenic influence on a summertime heat stress index. Clim. Chang. 138, 25–39. http://dx.doi.org/10.1007/s10584-016-1708-z.

LeComte, D., 2014. International weather highlights 2013: super typhoon Haiyan, super heat in Australia and China, a long winter in Europe. Weatherwise 67 (3), 20–27. http://dx.doi.org/10.1080/00431672.2014.899800.

Lewis, S.C., Karoly, D.J., 2013. Anthropogenic contributions to Australia's record summer temperatures of 2013. Geophys. Res. Lett. 40, 3705–3709. http://dx.doi.org/10.1002/grl.50673.

Mahlstein, I., Knutti, R., Solomon, S., Portmann, R.W., 2011. Early onset of significant local warming in low latitude countries. Environ. Res. Lett. 6, 034009.

McSweeney, C.F., Jones, R.G., Lee, R.W., Rowell, D.P., 2015. Selecting CMIP5 GCMs for downscaling over multiple regions. Clim. Dyn. 44, 3237–3260 http://doi.org/10.1007/s00382-014-2418-8.

Mora, C., et al., 2017. Global risk of deadly heat. Nat. Clim. Chang. 7, 501–506. http://dx.doi.org/10.1038/nclimate3322.

Pal, J.S., Eltahir, E.A.B., 2016. Future temperature in Southwest Asia projected to exceed a threshold for human adaptability. Nat. Clim. Chang. 6, 197–200. http://dx.doi.org/10.1038/nclimate2833.

Pal, J.S., Giorgi, F., Bi, X., Elguindi, N., Solmon, F., Gao, X., Rauscher, S., Francisco, R., Zakey, A., Winter, J., Ashfaq, M., Syed, F.S., Bell, J.L., Diffenbaugh, N.S., Karmacharya, J., Konaré, A., Martinez, D., da Rocha, R.P., Sloan, L.C., Steiner, A.L., 2007. The ICTP RegCM3 and RegCNET: regional climate modeling for the developing world. Bull. Am. Meteorol. Soc. 88, 1395–1409. http://dx.doi.org/10.1175/BAMS-88-9-1395.

Schär, C., Vidale, P.L., Lüthi, D., Frei, C., Häberli, C., Liniger, M., Appenzeller, C., 2004. The role of increasing temperature variability in European summer heatwaves. Nature 427, 332–336.

Sherwood, S.C., Huber, M., 2010. An adaptability limit to climate change due to heat stress. Proc. Natl. Acad. Sci. 107 (21), 9552–9555. http://dx.doi.org/10.1073/pnas.0913352107.

Smith, K.R., et al., 2014. Human health: Impacts, adaptation, and co-benefits. In: Climate Change Volume 2014: Impacts, Adaptation, and Vulnerability. Part A: Global and Sectoral Aspects. Contribution of Working Group II to the Fifth Assessment Report of the Intergovernmental Panel on Climate Change. Cambridge University Press, Cambridge (709–754pp).

Stocker, T.F., et al., 2013. Technical summary. In: Climate Change 2013: The Physical Science Basis. Contribution of Working Group I to the Fifth Assessment Report of the Intergovernmental Panel on Climate Change. Cambridge University Press, Cambridge (1535 pp).

Wang, A., Zeng, X., 2013. Development of global hourly 0.5° land surface air temperature datasets. J. Clim. 26, 7676–7691.

Wilbanks, T., Fernandez, S., Backus, G., Garcia, P., Jonietz, K., Kirshen, P., Savonis, M., Solecki, B., Toole, L., 2012. Climate change and infrastructure, urban systems, and vulnerabilities: technical report for the U.S. Department of Energy in Support of the National Climate Assessment. http://www.ourenergypolicy.org/wp-content/

uploads/2014/03/document_cw_01.pdf.

Willett, K.M., Sherwood, S., 2012. Exceedance of heat index thresholds for 15 regions under a warming climate using the wet-bulb globe temperature. Int. J. Climatol. 32, 161–177. http://dx.doi.org/10.1002/joc.2257.

Yatagai, A., Kamiguchi, K., Arakawa, O., Hamada, A., Yasutomi, N., Kitoh, A., 2012. APHRODITE: constructing a long-term daily gridded precipitation dataset for Asia based on a dense network of rain gauges. Bull. Am. Meteorol. Soc. 93, 1401–1415.